Editors' Suggestion

Generation of High-Density High-Polarization Positrons via Single-Shot Strong Laser-Foil Interaction

Kun Xue,[1] Ting Sun,[1] Ke-Jia Wei,[1] Zhong-Peng Li,[1] Qian Zhao,[1] Feng Wan,[1,*] Chong Lv,[2,†] Yong-Tao Zhao,[1] Zhong-Feng Xu,[1] and Jian-Xing Li[1,2,‡]

[1]*Key Laboratory for Nonequilibrium Synthesis and Modulation of Condensed Matter (MOE), Shaanxi Province Key Laboratory of Quantum Information and Quantum Optoelectronic Devices, School of Physics, Xi'an Jiaotong University, Xi'an 710049, China*

[2]*Department of Nuclear Physics, China Institute of Atomic Energy, P.O. Box 275(7), Beijing 102413, China*

(Received 7 June 2023; accepted 19 September 2023; published 24 October 2023)

We put forward a novel method for producing ultrarelativistic high-density high-polarization positrons through a single-shot interaction of a strong laser with a tilted solid foil. In our method, the driving laser ionizes the target, and the emitted electrons are accelerated and subsequently generate abundant γ photons via the nonlinear Compton scattering, dominated by the laser. These γ photons then generate polarized positrons via the nonlinear Breit-Wheeler process, dominated by a strong self-generated quasistatic magnetic field $\mathbf{B}^{\mathrm{S}}$. We find that placing the foil at an appropriate angle can result in a directional orientation of $\mathbf{B}^{\mathrm{S}}$, thereby polarizing positrons. Manipulating the laser polarization direction can control the angle between the γ photon polarization and $\mathbf{B}^{\mathrm{S}}$, significantly enhancing the positron polarization degree. Our spin-resolved quantum electrodynamics particle-in-cell simulations demonstrate that employing a laser with a peak intensity of about 10^{23} W/cm^2 can obtain dense ($\gtrsim 10^{18}$ cm^{-3}) polarized positrons with an average polarization degree of about 70% and a yield of above 0.1 nC per shot. Moreover, our method is feasible using currently available or upcoming laser facilities and robust with respect to the laser and target parameters. Such high-density high-polarization positrons hold great significance in laboratory astrophysics, high-energy physics, and new physics beyond the standard model.

DOI: 10.1103/PhysRevLett.131.175101

Ultrarelativistic spin-polarized positrons find wide use in laboratory astrophysics, high-energy physics, and new physics beyond the standard model [1–6], such as simulating extreme cosmic environments in laboratories [5,7,8], precisely measuring the effective weak mixing angle [9,10], and searching for supersymmetry particles and gravitons [11–14]. These applications usually demand high density and high polarization of positrons. For example, relevant experiments in the International Linear Collider (ILC) [15], the Circular Electron Positron Collider [16], and the Jefferson Lab Electron Ion Collider [17] require dense (∼ nanocoulombs per shot) highly polarized (30% ∼ 60%) positrons. There are mainly two methods used in experiments to obtain ultrarelativistic polarized positrons. One is spontaneous polarization of positrons via the Sokolov-Ternov effect in storage rings, but it typically takes several minutes to hours due to the relatively weak magnetic field (∼Tesla) [18]. Another is the Bethe-Heitler (BH) electron-positron pair production [19] in the interaction of circularly polarized γ photons with high-Z targets [20–22], but the average polarization degree of positrons is only 30% ∼ 40% and the positron yield is limited to 10^{-6} nC per shot due to the low luminosity of γ photon beams [23,24].

The rapid development of modern ultraintense ultrashort laser facilities, with a record intensity of above 10^{23} W/cm^2 [25–28], has led to the proposals of generating polarized positrons through laser-electron beam collisions in the strong-field quantum electrodynamics (QED) regime [29–41]. This collision scheme mainly involves emitting γ photons via the nonlinear Compton scattering (NCS) and producing positrons via the nonlinear Breit-Wheeler (NBW) process in the laser field [42–48]. Positrons with a polarization degree of 30% ∼ 40% can be obtained by colliding an unpolarized GeV electron beam with an asymmetric laser pulse, such as an elliptically polarized [37] or bichromatic laser pulse [38]. However, the positron polarization degree is typically limited, since the parent photon polarization $\mathbf{P}_\gamma$ and the magnetic field $\mathbf{B}'$ in the positron rest frame are always nearly perpendicular (i.e., $\mathbf{P}_\gamma \perp \mathbf{B}'$). Positron polarization and yield are significantly influenced by the angle Θ between $\mathbf{P}_\gamma$ and $\mathbf{B}'$, reaching a maximum when $\mathbf{P}_\gamma \| \mathbf{B}'$ and minimum when $\mathbf{P}_\gamma \perp \mathbf{B}'$ [39,40,49–52]. Alternatively, positrons with a polarization degree of 40% ∼ 65% can be obtained by a fully longitudinally polarized GeV electron beam colliding with a circularly polarized laser pulse [41], but its applicability is limited by the flux and polarization of electron beams [53]. In the above laser-electron beam collision scheme, to achieve high density of positrons, dense GeV electron beams are envisioned to be obtained via plasma wakefield

acceleration [54–57], typically resulting in a yield of 10^{-4} nC per shot and a maximum density of $\sim 10^{14}$ cm^{-3} [38]. Moreover, achieving precise spatiotemporal synchronization between the laser and electron beams is also challenging.

By comparison, laser irradiation on solid targets can avoid the spatiotemporal synchronization issue and is predicted to produce dense positrons in the strong-field QED regime [58–68]. For instance, a 10 PW laser irradiating an aluminum foil can achieve a maximum positron density of $\sim 10^{20}$ cm^{-3} [58]. Meanwhile, polarized positrons can be generated by a laser with a peak intensity exceeding 10^{24} W/cm^2 normally irradiating a foil target [69]. In this method, positrons are polarized by an asymmetrical laser field in the skin layer of overdense plasma. However, the polarization degree is limited to about 30% due to the intrinsic geometric relationship $\mathbf{P}_\gamma \perp \mathbf{B}'$, similar to Refs. [37,38]. Therefore, it is still a great challenge to obtain dense polarized positrons with a high-polarization degree ($\gtrsim$60%).

In this Letter, we investigate the generation of ultrarelativistic high-density high-polarization positrons via single-shot laser-foil interaction in the strong-field QED regime; see Fig. 1(a). The driving laser ionizes the target and directly accelerates the emitted electrons [70–78], and these electrons then emit abundant γ photons via the NCS, which is dominated by the laser field. The emitted γ photons subsequently generate polarized positrons via the NBW process, which is dominated by a strong self-generated quasistatic magnetic field $\mathbf{B}^{\mathrm{S}}$. We find that placing the foil at an appropriate angle can result in a directional orientation of $\mathbf{B}^{\mathrm{S}}$ due to the electric currents along the foil surface [see Fig. 1(b)], thereby polarizing positrons. Manipulating the laser polarization direction can control the polarization of intermediate γ photons $\mathbf{P}_\gamma$ [see Fig. 1(c)], thereby controlling the angle Θ between $\mathbf{P}_\gamma$ and $\mathbf{B}^{\mathrm{S}}$ and significantly enhancing the polarization degree of positrons [see Fig. 1(d)]. Under the influence of $\mathbf{B}^{\mathrm{S}}$, most positrons move through the target, while newborn electrons propagate along the front surface of the target, ultimately mixing with unpolarized target electrons. Our three-dimensional spin-resolved QED particle-in-cell (PIC) simulations show that using a laser with a peak intensity of about 10^{23} W/cm^2 can obtain dense ($\gtrsim 10^{18}$ cm^{-3}) transversely polarized positrons with an average polarization degree of about 70% and a yield of above 0.1 nC per shot; see Fig. 2. Our method is feasible using currently available or upcoming laser facilities, as it avoids the need for exact spatiotemporal synchronization. Moreover, our method is robust with respect to the laser and target parameters; see the Appendix.

We utilize a Monte Carlo algorithm [37,39,79] in PIC code to investigate spin-resolved QED phenomena in laser-solid interactions. Two primary QED processes, NCS and NBW, are implemented in the local constant field

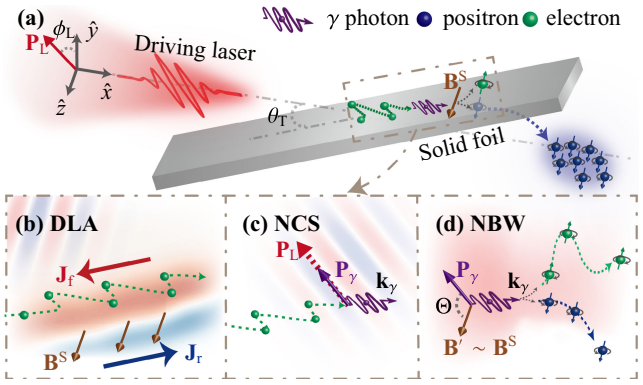

FIG. 1. (a) Interaction scenario. The laser propagates along $+\hat{x}$ and is polarized along $\mathbf{P}_{\mathrm{L}}$, with the laser polarization angle ϕ_{L} between $\mathbf{P}_{\mathrm{L}}$ and $+\hat{y}$; the foil has a tilt angle θ_{T} with respect to the $\hat{x}$-$\hat{z}$ plane. (b) Direct laser acceleration (DLA). The brown, red, and blue arrows represent the directional quasistatic magnetic field $\mathbf{B}^{\mathrm{S}}$, the surface electric current $\mathbf{J}_{\mathrm{f}}$, and the return current $\mathbf{J}_{\mathrm{r}}$, respectively; $\mathbf{J}_{\mathrm{f}}$ and $\mathbf{J}_{\mathrm{f}}$ are both parallel to the front surface of the target; $\mathbf{B}^{\mathrm{S}}$ is oriented along $+\hat{z}$; the green-dotted line indicates the trajectory of the surface fast electrons; the heat maps in the top left and bottom right represent the incident laser field and the currents, respectively. (c) NCS process. The red and purple arrows represent the polarization of the laser and γ photons, respectively; $\mathbf{k}_\gamma$ is the γ photon wave vector; the heat map represents the reflected laser field, which propagates from left to right. (d) NBW process. The blue and green arrows represent the polarization directions of positrons and electrons, respectively, and the blue- and green-dotted lines represent their respective trajectories; the approximation of the magnetic field $\mathbf{B}'$ in the positron rest frame being equal to $\mathbf{B}^{\mathrm{S}}$ is employed; the heat map represents $\mathbf{B}^{\mathrm{S}}$.

approximation [30,31,34], which is valid for the invariant field parameter $a_0 \equiv |e|E_0/mc\omega_0 \gg 1$. These processes are characterized by two nonlinear QED parameters $\chi_e \equiv (|e|\hbar/m^3c^4)\sqrt{-(F_{\mu\nu}p^\nu)^2}$ and $\chi_\gamma \equiv (|e|\hbar/m^3c^4)\sqrt{-(F_{\mu\nu}k^\nu)^2}$ [30,31], respectively. Here e and m are electron charge and mass, respectively, E_0 and ω_0 are laser field amplitude and frequency, respectively, c is the light speed in vacuum, $\hbar$ is the reduced Planck constant, k^ν and p^ν are the 4-momenta of γ photon and electron (positron), respectively, and $F_{\mu\nu}$ is the field tensor.

Typical results are shown in Fig. 2. The simulation box has dimensions of $x \times y \times z = 40\ \mu\mathrm{m} \times 40\ \mu\mathrm{m} \times 30\ \mu\mathrm{m}$, with the corresponding cells of $1000 \times 1000 \times 750$. A linearly polarized laser pulse propagates along $+\hat{x}$, with a polarization angle $\phi_{\mathrm{L}} = 45°$ [see Fig. 1(a)], wavelength $\lambda_0 = 1\ \mu\mathrm{m}$, and an envelope $a = a_0 \exp(-r^2/w_0^2)\exp[-(t-t_0)^2/\tau^2]$. Here $a_0 = 500$ [a smaller a_0 also works; see Fig. 4(c) in the Appendix] with a corresponding peak intensity of 3.4×10^{23} W/cm^2, which can be achieved in upcoming 10 or 100 PW laser facilities [26,80–86], $r = \sqrt{y^2+z^2}$, $w_0 = 5\lambda_0$ is the focal

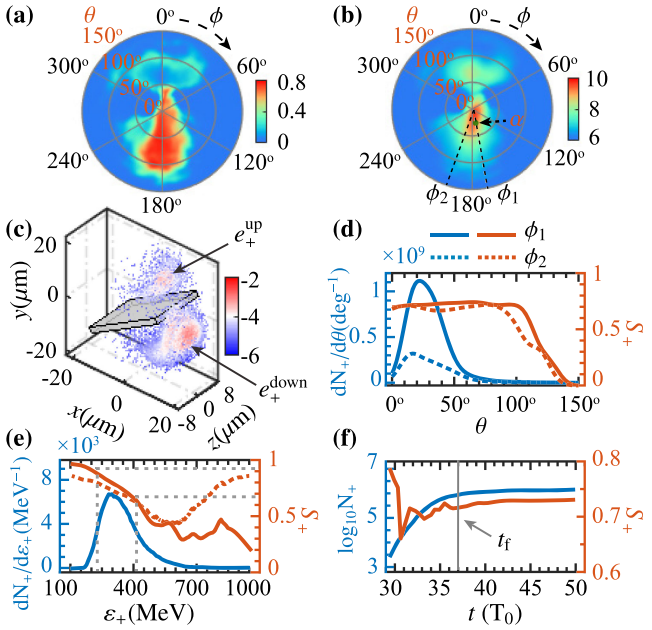

FIG. 2. (a) Angle-resolved positron polarization S_+ and (b) distribution $\log_{10}(dN_+/d\Omega)$ with respect to the polar angle θ and the azimuth angle ϕ, respectively. Here $d\Omega = \sin\theta d\theta d\phi$, $\theta = 0°$ in $+\hat{x}$, and $\phi = 0°$ in $+\hat{y}$. (c) Positron density $\log_{10}(n_+/n_c)$. The gray box represents the initial position of the foil; e_+^{down} represents positrons propagating downward through the target, while e_+^{up} represents positrons propagating upward along the target surface. (d) Positron angle distribution $dN_+/d\theta$ and polarization S_+ vs θ at $\phi_1 = 176°$ (solid lines) and $\phi_2 = 200°$ (dotted lines). Here we collect positrons within a range of $\Delta\phi = 1°$. (e) Energy-resolved positron density $dN_+/d\varepsilon_+$ and polarization S_+ vs positron energy ε_+ at α. The gray-dotted lines indicate the FWHM of positron energy; the red-dotted line represents the results of neglecting the radiative polarization effects of positrons. All above results are at simulation time $t = 50T_0$. (f) Positron yield $\log_{10} N_+$ and polarization S_+ vs t at α. $t_f = 37T_0$ is the time of laser departure.

radius, $\tau = 6T_0$ is the pulse duration with a corresponding full width at half maximum (FWHM) $\tau' \approx 10T_0$, T_0 is the laser period, and $t_0 = 12T_0$ is the time delay. (t_0 is used to shift the laser pulse out of the simulation box at time $t = 0$.) A carbon foil with electron density $n_e = 550n_c$, length $L_T = 30$ μm, and thickness $d_T = 2$ μm is placed in the box center at a tilt angle $\theta_T = 30°$, where $n_c = m\omega_0^2/(4\pi e^2) \approx 1.1 \times 10^{21}$ cm^{-3} is the plasma critical density. Note that low-Z target materials are required to effectively suppress the BH process [19]. Accounting for pulse leading edge or a prepulse [87], a preplasma with density $n_{pre} = n_e \exp(-L/L_{pre})$ is used. Here L is the distance between preplasma particles and the front surface of the target, and $L_{pre} = 0.5$ μm is the preplasma scale length. The numbers of macroparticles in each cell are 30 for electrons and 15 for fully ionized C^{6+}.

The yield of positrons generated via the NBW process is roughly 8.0×10^8 (~0.13 nC), which is about 2 orders of magnitude larger than that of the BH process (~1.7×10^6) (see Supplemental Material [88]), and thus the contribution of the BH process is negligible. Most positrons (7.5×10^8 $e^+ \sim 0.12$ nC) travel downward the target [see e_+^{down} in Fig. 2(c)], with an average polarization degree of 67.3%, while a small amount propagate upward in the front of the target [see e_+^{up} in Fig. 2(c)], with a slight polarization degree (~5.0%); see Figs. 2(a) and 2(b). Their distinct polarization properties arise from their different birth regions; see the reasons in Fig. 3. As shown in Fig. 2(c), the maximum positron density is above $10^{-3}n_c \approx 10^{18}$ cm^{-3}, which is 4 orders of magnitude higher than these typically achieved in laser-electron beam collision schemes [37,38,41]. At the peak angle of $\phi = 176°$, the positron polarization degree remains above 70% for $0° < \theta < 100°$; see Fig. 2(d). Similar phenomena are observed at $\phi = 200°$. The high polarization of positrons over a wide range of angles can be beneficial for detection.

Considering the capture and transfer of positrons for subsequent applications, we will focus on positrons within the peak cone angle $\alpha = (25° < \theta < 27°, 175° < \phi 177°)$; see Fig. 2(b). These positrons have an average polarization degree of about 72.3%. Their polarization degree S_+ decreases from 88.1% to 62.6% within the FWHM energy range of 225 MeV $< \varepsilon_+ <$ 416 MeV, and $S_+ \approx 79.4\%$ at the energy peak of $\varepsilon_+ \approx 300$ MeV; see Fig. 2(e). These positrons have a yield of 1×10^6 (~0.2 pC), a flux of about 2×10^9 sr^{-1}, and an angle divergence of 35×35 mrad^2, with transverse and longitudinal sizes of $3 \times 1.5\mu m^2$ and 2 μm (at $t = 50T_0$), respectively; see the comparisons with alternative sources in the Appendix. In principle, these positrons are suitable for injection into subsequent acceleration, such as radio-frequency accelerator and plasma wakefield acceleration [89–91], owing to their sufficient charge and low divergence. Particularly, the small spatial size is desirable for injecting positrons in plasma wakefield acceleration due to the limited acceleration range of a few microns [90,91]. The brilliances are 0.65×10^{19}, 0.55×10^{20}, 0.42×10^{20}, and 0.17×10^{20} $e_+/(\text{s mm}^2\,\text{mrad}^2 \times 0.1\%\ \text{bandwidth})$ for $\varepsilon_+ = 200$, 300, 400, and 500 MeV, respectively. As shown in Fig. 2(f), positrons are mainly produced during laser irradiation ($27T_0 < t < 37T_0$), and their yield and polarization tend to stabilize after the laser departs. Moreover, the radiative polarization effects can enhance the polarization of the low-energy positrons as they pass through the directional magnetic field $\mathbf{B}^S$; see the results of artificially neglecting the radiative polarization effects in Fig. 2(e) and the corresponding reasons in Fig. 3(e). Additionally, the newborn electrons exhibit a high initial polarization, which gradually diminishes to a polarization degree of approximately 10% due to the depolarization effects derived from the spin precession and the radiation during their propagation along the target surface [88,92].

The mechanisms for the production and polarization of positrons are shown in Fig. 3. Upon laser irradiation,

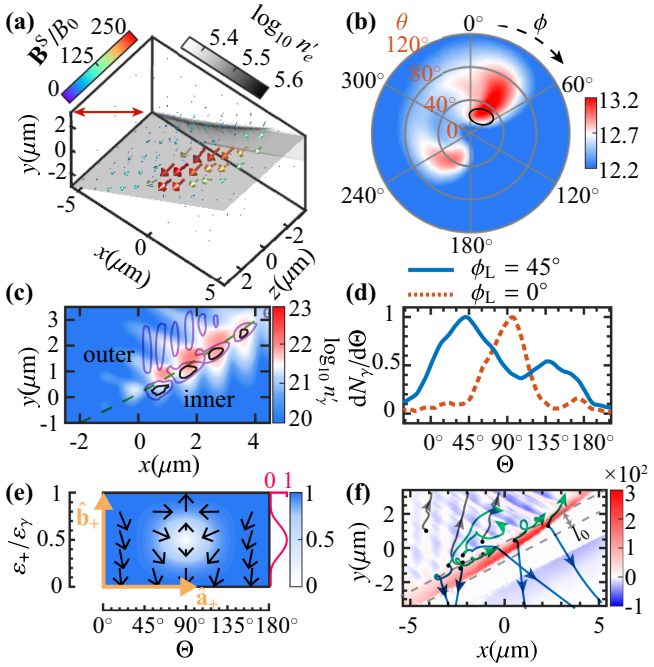

FIG. 3. (a) $\mathbf{B}^S/B_0$ and projection of electron density $\log_{10}(n'_e)$ in the $\hat{x}$-$\hat{y}$ plane. The red bidirectional arrow represents the laser polarization direction. (b) Angle distribution of γ photons $\log_{10}(dN_\gamma/d\Omega)$ with respect to θ and ϕ. Positron production mainly occurs within the black circle region ($10° < \theta < 30°$, $0° < \phi < 60°$) [88]. (c) Projection of photon density $\log_{10}(n'_\gamma)$ for photon energy $\varepsilon_\gamma > 300$ MeV in the $\hat{x}$-$\hat{y}$ plane. The green-dashed line represents the front surface of the target; the black and purple lines represent the contour lines of the average nonlinear QED parameter $\bar{\chi}_\gamma = 0.35$ and $\bar{\chi}_\gamma = 0.15$, respectively. (d) Polarization-resolved distribution of γ photons $dN_\gamma/d\Theta$ vs Θ. $\mathbf{B}' \approx \varepsilon_+[\mathbf{B}^S\text{-}\hat{\mathbf{v}}_+(\hat{\mathbf{v}}_+ \cdot \mathbf{B}^S)]$ and $\mathbf{B}^S \| + \hat{\mathbf{z}}$ are employed; the γ photons originate from the peak cone angles ($19° < \theta < 21°$, $-1° < \phi < 1°$) and ($24° < \theta < 26°$, $25° < \phi < 27°$) for the cases of $\phi_L = 0°$ (red dotted) and $\phi_L = 45°$ (blue solid), respectively. (e) $|\bar{\mathbf{S}}_+|$ with respect to Θ and $\varepsilon_+/\varepsilon_\gamma$. The black arrows represent $\bar{\mathbf{S}}_+$; the red line indicates the pair creation probability $dW/d(\varepsilon_+/\varepsilon_\gamma)$ for $\Theta = 90°$, normalized by its maximum; $\chi_\gamma = 0.4$ is employed. (f) Projection of B^S_z/B_0 in the $\hat{x}$-$\hat{y}$ plane. The blue, green, and gray lines with arrows represent trajectories of the downward positrons e^{down}_+, the newborn electrons, and the upward positrons e^{up}_+, respectively; l_0 is the spatial dimension of $\mathbf{B}^S$. All of the above simulation results are at $t = 35T_0$.

electrons are accelerated through $\mathbf{J} \times \mathbf{B}$ heating [93,94] to form a fast electron current $\mathbf{J}_f$ parallel to the front surface of the target; and a return current $\mathbf{J}_r$ of cold electrons also appears inside the target to maintain charge balance, with a direction opposite to $\mathbf{J}_f$ [75,76,95]; see Fig. 1(b). Therefore, a quasistatic magnetic field $\mathbf{B}^S$ is generated and oriented along $+\hat{z}$, with a peak strength $B^S_{max} \approx 250B_0 \approx 2.5 \times 10^6$ T, which is of the same order of magnitude as the magnetic field of the laser; see Fig. 3(a). Here $B_0 = m\omega_0/|e| \approx 1 \times 10^4$ T. The high-density electron layer on the front surface of the target can divide the space into an outer region and an inner region; see Fig. 3(c). In the inner region, the laser field rapidly decays within the skin depth and $\mathbf{B}^S$ dominates the pair creation. When considering only $\mathbf{B}^S$, one has $\chi_\gamma \sim 0.36$, resulting in abundant positron production. Here $\mathbf{B}^S \sim (0, 0, B^S_z) \approx (0, 0, 200B_0)$, $\hat{\mathbf{k}}_\gamma$ along $(\theta, \phi) = (25°, 26°)$, and $\varepsilon_\gamma = 400$ MeV are employed (see Supplemental Material [88]). In contrast, in the outer region, the laser field is much stronger than $\mathbf{B}^S$, and the angle θ_0 between the wave vectors of the laser and γ photons is small. Therefore, $\chi_\gamma \propto a_0(1 - \cos\theta_0)$ is typically small, leading to fewer pair creations than that of the inner region. Our simulations also support the difference in positron yields between the two regions, indicating that positron production mainly occurs for γ photons that incident at a small angle with respect to the front surface of the target; see Fig. 3(b).

In addition to dominating the positron production, $\mathbf{B}^s$ also leads to the positron polarization. The average positron polarization $\bar{\mathbf{S}}_+$ can be written as [39]

$$\bar{\mathbf{S}}_+ = \frac{-\left(\frac{\varepsilon_\gamma}{\varepsilon_+} - \xi_3\frac{\varepsilon_\gamma}{\varepsilon_-}\right)K_{\frac{1}{3}}(\rho)\hat{\mathbf{b}}_+ + \xi_1\frac{\varepsilon_\gamma}{\varepsilon_-}K_{\frac{1}{3}}(\rho)\hat{\mathbf{a}}_+}{\mathrm{Int}K_{\frac{1}{3}}(\rho) + \frac{\varepsilon_+^2+\varepsilon_-^2}{\varepsilon_+\varepsilon_-}K_{\frac{2}{3}}(\rho) - \xi_3 K_{\frac{2}{3}}(\rho)}, \quad (1)$$

where $\varepsilon_- = \varepsilon_\gamma - \varepsilon_+$ is the energy of newborn electrons, $\rho = 2\varepsilon_\gamma^2/(3\chi_\gamma\varepsilon_-\varepsilon_+)$, $\mathrm{Int}K_{\frac{1}{3}}(\rho) \equiv \int_\rho^\infty dz K_{\frac{1}{3}}(z)$, K_n is the n-order modified Bessel function of the second kind, $\hat{\mathbf{b}}_+ = \hat{\mathbf{v}}_+ \times \hat{\mathbf{a}}_+/|\hat{\mathbf{v}}_+ \times \hat{\mathbf{a}}_+| \approx -\mathbf{B}'/|\mathbf{B}'|$ with $\mathbf{B}' \approx \varepsilon_+[\mathbf{B} - \hat{\mathbf{v}}_+ \times \mathbf{E}\text{-}\hat{\mathbf{v}}_+(\hat{\mathbf{v}}_+ \cdot \mathbf{B})]$, $\hat{\mathbf{v}}_+$ and $\hat{\mathbf{a}}_+$ are the unit vectors along positron velocity and acceleration, respectively, and $\mathbf{E}$ and $\mathbf{B}$ are the electric and magnetic fields, respectively. The photon polarization is characterized by the Stokes parameters $(\xi_1, \xi_2, \xi_3) \approx (\sin 2\Theta, 0, -\cos 2\Theta)$ [96] defined with respect to the axes $\hat{\mathbf{e}}_1 \equiv [\mathbf{E} - \hat{\mathbf{k}}_\gamma(\hat{\mathbf{k}}_\gamma \cdot \mathbf{E}) + \hat{\mathbf{k}}_\gamma \times \mathbf{B}]/|\mathbf{E} - \hat{\mathbf{k}}_\gamma(\hat{\mathbf{k}}_\gamma \cdot \mathbf{E}) + \hat{\mathbf{k}}_\gamma \times \mathbf{B}|$ and $\hat{\mathbf{e}}_2 \equiv \hat{\mathbf{k}}_\gamma \times \hat{\mathbf{e}}_1 \| \mathbf{B}'$, $\hat{\mathbf{k}}_\gamma = \mathbf{k}_\gamma/|\mathbf{k}_\gamma|$, and $\hat{\mathbf{v}}_+ \approx \hat{\mathbf{k}}_\gamma$ is employed (the emission angle $\sim mc^2/\varepsilon_\gamma \ll 1$ [19]). As shown in Fig. 3(e), $\bar{\mathbf{S}}_+$ always tends to align along $-\hat{\mathbf{b}}_+$, except in the vicinity of $\Theta = 90°$, where the reversal of $\bar{\mathbf{S}}_+$ around $\varepsilon_+/\varepsilon_\gamma = 0.5$ results in a low average polarization degree. In the outer region, the temporal symmetry of the laser leads to roughly equal positron yields in each half cycle of the laser, but the positron polarization direction reverses with the reversal of the laser magnetic field direction, resulting in zero net polarization. In contrast, in the inner region, the directionality of $\mathbf{B}' \sim \mathbf{B}^s$ can lead to net polarization. Furthermore, due to the Lorentz force exerted by $\mathbf{B}^S$, the positrons generated in the inner region mainly move through the target, i.e., the downward positrons e^{down}_+; see the blue lines with arrows in Fig. 3(f). Meanwhile, dominated by the laser field, the positrons produced in the outer region mainly

propagate in the front of the target, i.e., the upward positrons e_+^{up}; see the gray lines with arrows in Fig. 3(f).

As previously discussed, the average polarization degree of positrons $\bar{S}_+$ is low when $\Theta = 90°$, whereas a high $\bar{S}_+$ can be obtained when $\Theta = 45°$; see Fig. 3(e). Note that Θ can be manipulated by the laser polarization angle ϕ_{L}. For most γ photons, $\phi_{\mathrm{L}} + \Theta \approx 90°$. As shown in Fig. 3(d), for the cases of $\phi_{\mathrm{L}} = 0°$ (p-polarized laser incident) and $\phi_{\mathrm{L}} = 45°$, the γ photons are mainly distributed around $\Theta = 90°$ and 45°, respectively, leading to $\bar{S}_+ \approx 37\%$ and 70%, respectively [88]. However, as ϕ_{L} further increases, the polarization degree of γ photons will decrease and the manipulation of Θ will be weaker.

Furthermore, as positrons pass through the directional magnetic field $\mathbf{B}^{\mathrm{S}}$, the polarization effects of radiation cause positron spins to align preferentially with $\mathbf{B}^{\mathrm{S}}$. For positrons with $\varepsilon_+/\varepsilon_\gamma < 0.5$, $\bar{\mathbf{S}}_+$ at the positron creation moment is almost along $-\hat{\mathbf{b}}_+ \sim \mathbf{B}^{\mathrm{S}}$ [see Fig. 3(e)], leading to an increase in polarization upon radiation. On the contrary, for positrons with $\varepsilon_+/\varepsilon_\gamma > 0.5$, $\bar{\mathbf{S}}_+$ at the positron creation moment may not align with $\mathbf{B}^{\mathrm{S}}$ (such as $\Theta = 90°$ and 45°, where $\bar{\mathbf{S}}_+$ points toward $\hat{\mathbf{b}}_+ \sim -\mathbf{B}^{\mathrm{S}}$ and $+\hat{\mathbf{a}}$, respectively), leading to a decrease in polarization upon radiation. As a result, the average polarization degree $\bar{S}_+$ increases from 65.8% to 67.3%. Additionally, the depolarization caused by the spin precession of the downward positrons is relatively weak due to their rapid escape from the strong laser field under the influence of $\mathbf{B}^{\mathrm{S}}$ [88]. The γ photon attenuation (such as incoherent scatter, BH process, etc.) and the positron annihilation and collisions with other particles (such as Bhabha scattering, positron-nucleus scattering, etc.) during their propagation are estimated to be negligible [31,88,97].

For experimental feasibility, the impact of laser and target parameters on the yield N_+ and average polarization degree $\bar{S}_+$ of the downward positrons e_+^{down} has been investigated in the Appendix, which shows that our method is robust with respect to the foil tilt angle θ_{T}, the laser polarization angle ϕ_{L}, the laser peak intensity a_0, and the preplasma scale length L_{pre}. Moreover, the target configuration can also influence N_+ and $\bar{S}_+$. For example, using a conical target with the same laser pulse can remarkably increase the positron yield up to above 10 nC, but at the cost of reducing positron polarization [88]. Additionally, the experimental implementation of a submicron preplasma usually requires a temporal contrast of about $10^{-13} \sim 10^{-14}$ for ultraintense lasers with a peak intensity of about 10^{23} W/cm^2 [88,98], which would be generated in the near future via the utilization of plasma mirrors [99,100], plasma shutters [101], frequency conversion [102], etc.

In conclusion, we put forward a novel method for generating ultrarelativistic high-density high-polarization positrons in the single-shot laser-foil interaction, simply by manipulating the laser polarization and the foil placement to generate a proper positron polarization field. The positrons generated by our method may be widely used in laboratory astrophysics, high-energy physics, and new physics beyond the standard model, such as probing the spin-parity properties of hadrons [103] and providing an alternative polarized positron source for polarized electron-positron colliders.

This work is supported by the National Natural Science Foundation of China (Grants No. U2267204, No. 12022506, No. 12005305, and No. 12275209), the Foundation of Science and Technology on Plasma Physics Laboratory (No. JCKYS2021212008 and No. 6142A04220107), the Open Foundation of Key Laboratory of High Power Laser and Physics, Chinese Academy of Sciences (SGKF202101), the Shaanxi Fundamental Science Research Project for Mathematics and Physics (Grant No. 22JSY014), the Fundamental Research Funds for the Central Universities (No. xzy012023046), and the Foundation, China Institute of Atomic Energy under Grants No. FY222506000201 and No. FC232412000201.

Appendix: The experimental feasibility and positron qualities.—For experimental feasibility, the impact of laser and target parameters on the yield N_+ and average polarization degree $\bar{S}_+$ of the downward positrons e_+^{down} has been investigated in Fig. 4. The target tilt angle θ_{T} can affect the acceleration efficiency and angular distribution of fast electrons [76,95] and also affect the direction and magnitude of the quasistatic magnetic field $\mathbf{B}^{\mathrm{S}}$ [70], thereby further influencing N_+ and $\bar{S}_+$. If θ_{T} is too small, the energy coupling efficiency between the laser and the target will be low, resulting in a weak quasistatic magnetic field $\mathbf{B}^{\mathrm{S}}$ [74]. Consequently, both the polarization degree $\bar{S}_+$ and yield N_+ of positrons will be low; see Fig. 4(a). On the other hand, if θ_{T} is too large, the propagation of fast electron current $\mathbf{J}_{\mathrm{f}}$ will gradually change from propagating along the front surface of the target to propagating into the target bulk, resulting in oscillations of $\mathbf{B}^{\mathrm{S}}$ along $\hat{\mathbf{z}}$ and a reduction in its magnitude; see the magnitude and direction of $\mathbf{B}^{\mathrm{S}}$ at $\theta_{\mathrm{T}} = 70°$ in the Supplemental Material [88]. Meanwhile, the propagation directions of the reflected laser and γ photons change approximately from parallel to antiparallel, leading to the dominance of the reflected laser in pair production. Because of the symmetry of the laser field, the positrons generated in the laser field are almost unpolarized. Thus, a too large θ_{T} will lead to a low $\bar{S}_+$. Our simulations show that, for the given parameters, a high-polarization degree can be achieved when $20° \lesssim \theta_{\mathrm{T}} \lesssim 30°$. Additionally, when θ_{T} increases slightly, $\mathbf{B}^{\mathrm{S}}$ dominates the positron creation and $N_+ \propto \chi_\gamma \propto \mathbf{B}^{\mathrm{S}}$ increases, while when θ_{T} increases largely, the reflected

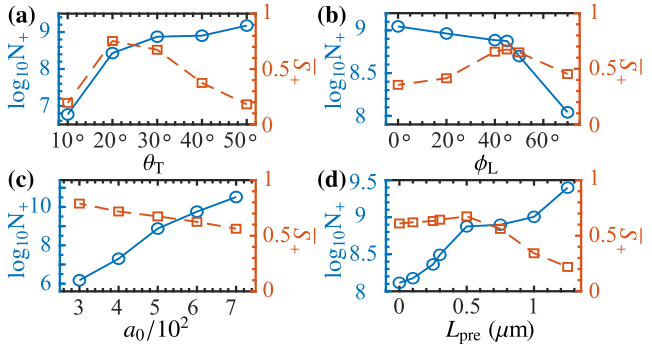

FIG. 4. The yield $\log_{10} N_+$ and average polarization degree $\bar{S}_+$ of the downward positrons e_+^{down} vs (a) the foil tilt angle θ_T, (b) the laser polarization angle ϕ_L, (c) the laser peak intensity a_0, and (d) the preplasma scale length L_{pre}, respectively. Other parameters are the same as those in Fig. 2.

laser dominates and $N_+ \propto \chi_\gamma \propto 1 - \cos\theta_0 \approx 1 - \cos(2\theta_T)$ increases. Consequently, as θ_T increases, N_+ increases.

Figure 4(b) shows the impact of the laser polarization angle ϕ_L on N_+ and $\bar{S}_+$. As ϕ_L increases, the coupling efficiency between the laser and the target decreases, leading to a decrease in the magnitude of $\mathbf{B}^S$ [70,73]. Consequently, $N_+ \propto \chi_\gamma \propto \mathbf{B}^S$ decreases. Moreover, as ϕ_L increases, the direction of γ photons $\mathbf{P}_\gamma$ gradually changes, leading to a reduction in the angle Θ between $\mathbf{P}_\gamma$ and $\mathbf{B}^S$ from 90°; see Fig. 3(d). As a result of this manipulation, $\bar{S}_+$ first increases. However, as ϕ_L further increases, the polarization degree of γ photons will decrease, resulting in a weakened manipulation of Θ, and thus $\bar{S}_+$ decreases. Precise experimental control of θ_T and ϕ_L can be achieved by adjusting the foil placement via a two-dimensional motor.

Figure 4(c) shows the impact of the laser peak intensity a_0 on N_+ and $\bar{S}_+$. In the strong-field QED regime, as the laser peak intensity a_0 increases, the surface electric current $\mathbf{J}_f$ also increases, resulting in strengthening $\mathbf{B}^S$. Thus, $N_+ \propto \chi_\gamma \propto \mathbf{B}^S$ increases. Nevertheless, an excessively strong laser will severely damage the target [104], leading to a decrease in $\bar{S}_+$ due to the arrival of some upward positrons e_+^{up} at the back of the target.

Figure 4(d) shows the impact of the preplasma scale length L_{pre} on N_+ and $\bar{S}_+$. Increasing the preplasma scale length L_{pre} can amplify the surface electric current $\mathbf{J}_f$, leading to an increase in the magnitude of $\mathbf{B}^S$, thereby enhancing N_+ and $\bar{S}_+$. However, when L_{pre} increases largely, especially when $L_{pre} > 0.5$ μm for the given parameters, the resonance absorption will gradually dominate the electron acceleration [74,75], resulting in the emergence of a strong current perpendicular to the target surface. Consequently, the directionality of $\mathbf{B}^S$ deteriorates [76,105], leading to a decrease in $\bar{S}_+$. Meanwhile, the spatial size of $\mathbf{B}^S$, i.e., l_0 [see Fig. 3(f)], will increase, leading to electron energy $\varepsilon_e \propto l_0^2$ increases [74,106], and thus $N_+ \propto \chi_\gamma \propto \varepsilon_\gamma \propto \varepsilon_e$ increases.

Additionally, to facilitate a comparison with alternative sources of positrons driven by ultraintense lasers, we present a more comprehensive description on the qualities of positrons generated through our method. For subsequent applications, positrons within the peak cone angle α will be taken into account; see the selection of α in Fig. 2(b). As shown in Fig. 2(e), these positrons have an average polarization degree greater than 70%, meeting the requirements for positron polarization in relevant experiments, such as ILC, which acquires an average polarization degree of ~60% [6]. In contrast, positrons generated through the BH methods [20–22] and laser-electron beam collision methods [37–41] typically have a polarization degree of 30% ~ 40%. In addition, the peak flux of the positrons within α is about 1.5×10^{20} e^+/s, which is higher than the typical peak flux of about $10^{17} \sim 10^{19}$ e^+/s generated by the laser-electron beam collision methods [37,38,41] and significantly higher than the typical peak flux of $10^{15} \sim 10^{16}$ e^+/s produced by the BH methods [20–22].

*wanfeng@xjtu.edu.cn
†lvchong@ciae.ac.cn
‡jianxing@xjtu.edu.cn

[1] Elliot Leader, *Spin in Particle Physics*, Cambridge Monographs on Particle Physics, Nuclear Physics, and Cosmology (Cambridge University Press, Cambridge, England, 2001).
[2] Igor Žutić, Jaroslav Fabian, and S. Das Sarma, Spintronics: Fundamentals and applications, Rev. Mod. Phys. **76**, 323 (2004).
[3] J. R. Danielson, D. H. E. Dubin, R. G. Greaves, and C. M. Surko, Plasma and trap-based techniques for science with positrons, Rev. Mod. Phys. **87**, 247 (2015).
[4] M. Ablikim, M. N. Achasov, S. Ahmed *et al.* (The BESIII Collaboration), Polarization and entanglement in baryon-antibaryon pair production in electron-positron annihilation, Nat. Phys. **15**, 631 (2019).
[5] Bruce A. Remington, R. Paul Drake, and Dmitri D. Ryutov, Experimental astrophysics with high power lasers and z pinches, Rev. Mod. Phys. **78**, 755 (2006).
[6] G. Moortgat-Pick, T. Abe, G. Alexander, B. Ananthanarayan, A. A. Babich, V. Bharadwaj, D. Barber, A. Bartl, A. Brachmann, Si Chen *et al.*, Polarized positrons and electrons at the linear collider, Phys. Rep. **460**, 131 (2008).
[7] O. P. Novak and R. I. Kholodov, Spin-polarization effects in the processes of synchrotron radiation and electron-positron pair production by a photon in a magnetic field, Phys. Rev. D **80**, 025025 (2009).
[8] Remo Ruffini, Gregory Vereshchagin, and She-Sheng Xue, Electron–positron pairs in physics and astrophysics: From heavy nuclei to black holes, Phys. Rep. **487**, 1 (2010).

[9] Alain Blondel, A scheme to measure the polarization asymmetry at the z pole in LEP, Phys. Lett. B **202**, 145 (1988).

[10] Abdelhak Djouadi, The anatomy of electroweak symmetry breaking: Tome I: The Higgs boson in the standard model, Phys. Rep. **457**, 1 (2008).

[11] E. Boos, H. U. Martyn, G. Moortgat-Pick, M. Sachwitz, A. Sherstnev, and P. M. Zerwas, Polarisation in sfermion decays: Determining $\tan\beta$ and trilinear couplings, Eur. Phys. J. C **30**, 395 (2003).

[12] Alfred Bartl, Stefan Hesselbach, Karl Hohenwarter-Sodek, Hans Fraas, and Gudrid Moortgat-Pick, A T-odd asymmetry in neutralino production and decay, J. High Energy Phys. 08 (2004) 038.

[13] S. Bornhauser, M. Drees, H. Dreiner, O. J. P. Éboli, J. S. Kim, and O. Kittel, CP asymmetries in the supersymmetric trilepton signal at the LHC, Eur. Phys. J. C **72**, 1887 (2012).

[14] Thomas G. Rizzo, Transverse polarization signatures of extra dimensions at linear colliders, J. High Energy Phys. 02 (2003) 008.

[15] Klaus Flöttmann, *Investigations toward the Development of Polarized and Unpolarized High Intensity Positron Sources for Linear Colliders* (DESY, Berlin, 1993), Vol. 93.

[16] Zhe Duan, Jie Gao, XP Li, Dou Wang, Yiwei Wang, Wenhao Xia, Qingjin Xu, Chenghui Yu, Yuan Zhang *et al.*, Concepts of longitudinally polarized electron and positron colliding beams in the circular electron positron collider, in *Proceedings of the 10th International Particle Accelerator Conference (IPAC'19), Melbourne, 2019* (JACOW Publishing, Geneva, Switzerland, 2019), pp. 445–448.

[17] Fanglei Lin, Joe Grames, Jiquan Guo, Vasiliy Morozov, and Yuhong Zhang, Polarized positrons in Jefferson Lab electron ion collider (JLEIC), AIP Conf. Proc. Vol. **1970**, 050005 (2018).

[18] S. R. Mane, Yu M. Shatunov, and K. Yokoya, Spin-polarized charged particle beams in high-energy accelerators, Rep. Prog. Phys. **68**, 1997 (2005).

[19] W. Heitler, *The Quantum Theory of Radiation* (Clarendon Press, Oxford, 1954).

[20] T. Omori, M. Fukuda, T. Hirose, Y. Kurihara, R. Kuroda, M. Nomura, A. Ohashi, T. Okugi, K. Sakaue, T. Saito, J. Urakawa, M. Washio, and I. Yamazaki, Efficient propagation of polarization from laser photons to positrons through Compton scattering and electron-positron pair creation, Phys. Rev. Lett. **96**, 114801 (2006).

[21] G. Alexander *et al.*, Observation of polarized positrons from an undulator-based source, Phys. Rev. Lett. **100**, 210801 (2008).

[22] D. Abbott, P. Adderley, A. Adeyemi *et al.* (PEPPo Collaboration), Production of highly polarized positrons using polarized electrons at MeV energies, Phys. Rev. Lett. **116**, 214801 (2016).

[23] J. Dumas, J. Grames, and E. Voutier, Polarized positrons at Jefferson Lab, AIP Conf. Proc. **1149**, 1184 (2009).

[24] Felix Dietrich, Gudrid Moortgat-Pick, Sabine Riemann, Peter Sievers, and Andriy Ushakov, Status of the undulator-based ILC positron source, arXiv:1902.07744.

[25] J. Kawanaka, K. Tsubakimoto, H. Yoshida, K. Fujioka, Y. Fujimoto, S. Tokita, T. Jitsuno, N. Miyanaga, and Gekko-EXA Design Team, Conceptual design of sub-exa-watt system by using optical parametric chirped pulse amplification, J. Phys. Conf. Ser. **688**, 012044 (2016).

[26] Edwin Cartlidge, The light fantastic, Science **359**, 382 (2018).

[27] Colin N. Danson, Constantin Haefner, Jake Bromage, Thomas Butcher, Jean-Christophe F. Chanteloup, Enam A. Chowdhury, Almantas Galvanauskas, Leonida A. Gizzi, Joachim Hein, David I. Hillier *et al.*, Petawatt and exawatt class lasers worldwide, High Power Laser Sci. Eng. **7**, e54 (2019).

[28] Jin Woo Yoon, Yeong Gyu Kim, Il Woo Choi, Jae Hee Sung, Hwang Woon Lee, Seong Ku Lee, and Chang Hee Nam, Realization of laser intensity over 10^{23} w/cm^2, Optica **8**, 630 (2021).

[29] Thomas Erber, High-energy electromagnetic conversion processes in intense magnetic fields, Rev. Mod. Phys. **38**, 626 (1966).

[30] V. I. Ritus, Quantum effects of the interaction of elementary particles with an intense electromagnetic field, J. Sov. Laser Res. **6**, 497 (1985).

[31] V. N. Baier, V. M. Katkov, and V. M. Strakhovenko, *Electromagnetic Processes at High Energies in Oriented Single Crystals* (World Scientific, Singapore, 1998).

[32] Yousef I. Salamin, S. X. Hu, Karen Z. Hatsagortsyan, and Christoph H. Keitel, Relativistic high-power laser–matter interactions, Phys. Rep. **427**, 41 (2006).

[33] Ting Sun, Qian Zhao, Kun Xue, Zhi-Wei Lu, Liang-Liang Ji, Feng Wan, Yu Wang, Yousef I. Salamin, and Jian-Xing Li, Production of polarized particle beams via ultraintense laser pulses, Rev. Mod. Plasma Phys. **6**, 38 (2022).

[34] A. Fedotov, A. Ilderton, F. Karbstein, B. King, D. Seipt, H. Taya, and G. Torgrimsson, Advances in QED with intense background fields, Phys. Rep. **1010**, 1 (2023).

[35] A. Di Piazza, C. Müller, K. Z. Hatsagortsyan, and Ch. H. Keitel, Extremely high-intensity laser interactions with fundamental quantum systems, Rev. Mod. Phys. **84**, 1177 (2012).

[36] A. Gonoskov, T. G. Blackburn, M. Marklund, and S. S. Bulanov, Charged particle motion and radiation in strong electromagnetic fields, Rev. Mod. Phys. **94**, 045001 (2022).

[37] Feng Wan, Rashid Shaisultanov, Yan-Fei Li, Karen Z. Hatsagortsyan, Christoph H. Keitel, and Jian-Xing Li, Ultrarelativistic polarized positron jets via collision of electron and ultraintense laser beams, Phys. Lett. B **800**, 135120 (2020).

[38] Yue-Yue Chen, Pei-Lun He, Rashid Shaisultanov, Karen Z. Hatsagortsyan, and Christoph H. Keitel, Polarized positron beams via intense two-color laser pulses, Phys. Rev. Lett. **123**, 174801 (2019).

[39] Kun Xue, Ren-Tong Guo, Feng Wan, Rashid Shaisultanov, Yue-Yue Chen, Zhong-Feng Xu, Xue-Guang Ren, Karen Z. Hatsagortsyan, Christoph H. Keitel, and Jian-Xing Li, Generation of arbitrarily polarized GeV lepton beams via nonlinear Breit-Wheeler process, Fundam. Res. **2**, 539 (2022).

[40] Ya-Nan Dai, Bai-Fei Shen, Jian-Xing Li, Rashid Shaisultanov, Karen Z. Hatsagortsyan, Christoph

H. Keitel, and Yue-Yue Chen, Photon polarization effects in polarized electron–positron pair production in a strong laser field, Matter Radiat. Extremes **7**, 014401 (2022).
[41] Yan-Fei Li, Yue-Yue Chen, Wei-Min Wang, and Hua-Si Hu, Production of highly polarized positron beams via helicity transfer from polarized electrons in a strong laser field, Phys. Rev. Lett. **125**, 044802 (2020).
[42] Bai Song Xie, Zi Liang Li, and Suo Tang, Electron-positron pair production in ultrastrong laser fields, Matter Radiat. Extremes **2**, 225 (2017).
[43] Marija Vranic, Ondrej Klimo, Georg Korn, and Stefan Weber, Multi-GeV electron-positron beam generation from laser-electron scattering, Sci. Rep. **8**, 4702 (2018).
[44] Yuan Zhao, Jianxun Liu, Yangmei Li, and Guoxing Xia, Ultra-bright γ-ray emission by using PW laser irradiating solid target obliquely, Plasma Phys. Controlled Fusion **61**, 065010 (2019).
[45] Victor Dinu and Greger Torgrimsson, Approximating higher-order nonlinear QED processes with first-order building blocks, Phys. Rev. D **102**, 016018 (2020).
[46] Yan-Fei Li, Rashid Shaisultanov, Yue-Yue Chen, Feng Wan, Karen Z. Hatsagortsyan, Christoph H. Keitel, and Jian-Xing Li, Polarized ultrashort brilliant multi-GeV γ rays via single-shot laser-electron interaction, Phys. Rev. Lett. **124**, 014801 (2020).
[47] Kun Xue, Zhen-Ke Dou, Feng Wan, Tong-Pu Yu, Wei-Min Wang, Jie-Ru Ren, Qian Zhao, Yong-Tao Zhao, Zhong-Feng Xu, and Jian-Xing Li, Generation of highly-polarized high-energy brilliant γ-rays via laser-plasma interaction, Matter Radiat. Extremes **5**, 054402 (2020).
[48] Greger Torgrimsson, Loops and polarization in strong-field QED, New J. Phys. **23**, 065001 (2021).
[49] D. Y. Ivanov, G. L. Kotkin, and V. G. Serbo, Complete description of polarization effects in e^+e^- pair production by a photon in the field of a strong laser wave, Eur. Phys. J. C **40**, 27 (2005).
[50] B. King, N. Elkina, and H. Ruhl, Photon polarization in electron-seeded pair-creation cascades, Phys. Rev. A **87**, 042117 (2013).
[51] D. Seipt and B. King, Spin- and polarization-dependent locally-constant-field-approximation rates for nonlinear Compton and Breit-Wheeler processes, Phys. Rev. A **102**, 052805 (2020).
[52] Feng Wan, Yu Wang, Ren-Tong Guo, Yue-Yue Chen, Rashid Shaisultanov, Zhong-Feng Xu, Karen Z. Hatsagortsyan, Christoph H. Keitel, and Jian-Xing Li, High-energy γ-photon polarization in nonlinear Breit-Wheeler pair production and γ polarimetry, Phys. Rev. Res. **2**, 032049(R) (2020).
[53] P. A. Adderley, J. Clark, Joe Grames, John Hansknecht, K. Surles-Law, D. Machie, M. Poelker, M. L. Stutzman, and Rafiu Suleiman, Load-locked dc high voltage GaAs photogun with an inverted-geometry ceramic insulator, Phys. Rev. ST Accel. Beams **13**, 010101 (2010).
[54] Cristian Bonţoiu, Öznur Apsimon, Egidijus Kukstas, Volodymyr Rodin, Monika Yadav, Carsten Welsch, Javier Resta-López, Alexandre Bonatto, and Guoxing Xia, TeV/m catapult acceleration of electrons in graphene layers, Sci. Rep. **13**, 1330 (2023).
[55] A. Pukhov and J. Meyer-ter-Vehn, Laser wake field acceleration: The highly non-linear broken-wave regime, Appl. Phys. B **74**, 355 (2002).
[56] Myung Hoon Cho, Vishwa Bandhu Pathak, Hyung Taek Kim, and Chang Hee Nam, Controlled electron injection facilitated by nanoparticles for laser wakefield acceleration, Sci. Rep. **8**, 16924 (2018).
[57] Edda Gschwendtner and Patric Muggli, Plasma wakefield accelerators, Nat. Rev. Phys. **1**, 246 (2019).
[58] C. P. Ridgers, Christopher S. Brady, R. Duclous, J. G. Kirk, K. Bennett, T. D. Arber, A. P. L. Robinson, and A. R. Bell, Dense electron-positron plasmas and ultraintense γ rays from laser-irradiated solids, Phys. Rev. Lett. **108**, 165006 (2012).
[59] Y. J. Gu, O. Klimo, S. Weber, and G. Korn, High density ultrashort relativistic positron beam generation by laser-plasma interaction, New J. Phys. **18**, 113023 (2016).
[60] Yan-Jun Gu, Ondrej Klimo, Sergei V Bulanov, and Stefan Weber, Brilliant gamma-ray beam and electron–positron pair production by enhanced attosecond pulses, Commun. Phys. **1**, 93 (2018).
[61] L. L. Ji, A. Pukhov, I. Yu. Kostyukov, B. F. Shen, and K. Akli, Radiation-reaction trapping of electrons in extreme laser fields, Phys. Rev. Lett. **112**, 145003 (2014).
[62] I. Yu. Kostyukov and E. N. Nerush, Production and dynamics of positrons in ultrahigh intensity laser-foil interactions, Phys. Plasmas **23**, 093119 (2016).
[63] Xing-Long Zhu, Tong-Pu Yu, Zheng-Ming Sheng, Yan Yin, Ion Cristian Edmond Turcu, and Alexander Pukhov, Dense GeV electron–positron pairs generated by lasers in near-critical-density plasmas, Nat. Commun. **7**, 13686 (2016).
[64] Jin-Jin Liu, Tong-Pu Yu, Yan Yin, Xing-Long Zhu, and Fu-Qiu Shao, All-optical bright γ-ray and dense positron source by laser driven plasmas-filled cone, Opt. Express **24**, 15978 (2016).
[65] Han-Zhen Li, Tong-Pu Yu, Li-Xiang Hu, Yan Yin, De-Bin Zou, Jian-Xun Liu, Wei-Quan Wang, Shun Hu, and Fu-Qiu Shao, Ultra-bright γ-ray flashes and dense attosecond positron bunches from two counter-propagating laser pulses irradiating a micro-wire target, Opt. Express **25**, 21583 (2017).
[66] W. Y. Liu, W. Luo, T. Yuan, J. Y. Yu, M. Chen, and Z. M. Sheng, Enhanced pair plasma generation in the relativistic transparency regime, Phys. Plasmas **24**, 103130 (2017).
[67] Liang-qi Zhang, Shao-dong Wu, Hai-rong Huang, Hao-yang Lan, Wei-yuan Liu, Yu-chi Wu, Yue Yang, Zong-qing Zhao, Zhi-chao Zhu, and Wen Luo, Brilliant attosecond γ-ray emission and high-yield positron production from intense laser-irradiated nano-micro array, Phys. Plasmas **28**, 023110 (2021).
[68] Marko Filipovic and Alexander Pukhov, QED effects at grazing incidence on solid-state targets, Eur. Phys. J. D **76**, 187 (2022).
[69] Huai-Hang Song, Wei-Min Wang, and Yu-Tong Li, Dense polarized positrons from laser-irradiated foil targets in the QED regime, Phys. Rev. Lett. **129**, 035001 (2022).
[70] Y. Sentoku, H. Ruhl, K. Mima, R. Kodama, K. A. Tanaka, and Y. Kishimoto, Plasma jet formation and magnetic-field

generation in the intense laser plasma under oblique incidence, Phys. Plasmas **6**, 2855 (1999).
[71] C. Gahn, G. D. Tsakiris, A. Pukhov, J. Meyer-ter-Vehn, G. Pretzler, P. Thirolf, D. Habs, and K. J. Witte, Multi-MeV electron beam generation by direct laser acceleration in high-density plasma channels, Phys. Rev. Lett. **83**, 4772 (1999).
[72] N. Naumova, I. Sokolov, J. Nees, A. Maksimchuk, V. Yanovsky, and G. Mourou, Attosecond electron bunches, Phys. Rev. Lett. **93**, 195003 (2004).
[73] Tatsufumi Nakamura, Susumu Kato, Hideo Nagatomo, and Kunioki Mima, Surface-magnetic-field and fast-electron current-layer formation by ultraintense laser irradiation, Phys. Rev. Lett. **93**, 265002 (2004).
[74] Tatsufumi Nakamura, Kunioki Mima, Hitoshi Sakagami, and Tomoyuki Johzaki, Electron surface acceleration on a solid capillary target inner wall irradiated with ultraintense laser pulses, Phys. Plasmas **14**, 053112 (2007).
[75] Min Chen, Zheng-Ming Shenga, Jun Zheng, Yan-Yun Ma, Muhammad Abbas Bari, Yu-Tong Li, and Jie Zhang, Surface electron acceleration in relativistic laser-solid interactions, Opt. Express **14**, 3093 (2006).
[76] Y. T. Li, X. H. Yuan, M. H. Xu, Z. Y. Zheng, Z. M. Sheng, M. Chen, Y. Y. Ma, W. X. Liang, Q. Z. Yu, Y. Zhang, F. Liu, Z. H. Wang, Z. Y. Wei, W. Zhao, Z. Jin, and J. Zhang, Observation of a fast electron beam emitted along the surface of a target irradiated by intense femtosecond laser pulses, Phys. Rev. Lett. **96**, 165003 (2006).
[77] Ye Tian, Jiansheng Liu, Wentao Wang, Cheng Wang, Aihua Deng, Changquan Xia, Wentao Li, Lihua Cao, Haiyang Lu, Hui Zhang, Yi Xu, Yuxin Leng, Ruxin Li, and Zhizhan Xu, Electron emission at locked phases from the laser-driven surface plasma wave, Phys. Rev. Lett. **109**, 115002 (2012).
[78] M. Thévenet, A. Leblanc, S. Kahaly, H. Vincenti, A. Vernier, F. Quéré, and Jérôme Faure, Vacuum laser acceleration of relativistic electrons using plasma mirror injectors, Nat. Phys. **12**, 355 (2016).
[79] Feng Wan, Chong Lv, Kun Xue, Zhen-Ke Dou, Qian Zhao, Mamutjan Ababekri, Wen-Qing Wei, Zhong-Peng Li, Yong-Tao Zhao, and Jian-Xing Li, Simulations of spin/polarization-resolved laser-plasma interactions in the nonlinear QED regime, Matter Radiat. Extremes **8**, 064002 (2023).
[80] Extreme Light Infrastructure (ELI), https://eli-laser.eu/.
[81] Exawatt Center for Extreme Light Studies (XCELS), https://xcels.iapras.ru/.
[82] Bruno Le Garrec, Stephane Sebban, Daniele Margarone, Martin Precek, Stefan Weber, Ondrej Klimo, Georg Korn, and Bedrich Rus, ELI-beamlines: Extreme light infrastructure science and technology with ultra-intense lasers, in *High Energy/Average Power Lasers and Intense Beam Applications VII*, edited by Steven J. Davis, Michael C. Heaven, and J. Thomas Schriempf, International Society for Optics and Photonics Vol. 8962 (SPIE, Bellingham, 2014), p. 89620I.
[83] Ji-Ping Zou, Catherine Le Blanc, Dimitrios N. Papadopoulos, Gilles Chériaux, Patrick Georges, G. Mennerat, Frédéric Druon, Ludovic Lecherbourg, Alain Pellegrina, Patricia Ramirez *et al.*, Design and current progress of the Apollon 10 PW project, High Power Laser Sci. Eng. **3**, e2 (2015).
[84] S. Gales *et al.*, The extreme light infrastructure–nuclear physics (ELI-NP) facility: New horizons in physics with 10 PW ultra-intense lasers and 20 MeV brilliant gamma beams, Rep. Prog. Phys. **81**, 094301 (2018).
[85] Zebiao Gan *et al.*, The Shanghai superintense ultrafast laser facility (SULF) project, in *Progress in Ultrafast Intense Laser Science XVI*, edited by Kaoru Yamanouchi, Katsumi Midorikawa, and Luis Roso (Springer International Publishing, Cham, 2021), pp. 199–217.
[86] Shuman Du, Xiong Shen, Wenhai Liang, Peng Wang, Jun Liu, and Ruxin Li, A 100-PW compressor based on single-pass single-grating pair, High Power Laser Sci. Eng. **11**, e4 (2023).
[87] Florian Wagner, Stefan Bedacht, Alex Ortner, Markus Roth, Anna Tauschwitz, Bernhard Zielbauer, and Vincent Bagnoud, Pre-plasma formation in experiments using petawatt lasers, Opt. Express **22**, 29505 (2014).
[88] See Supplemental Material at http://link.aps.org/supplemental/10.1103/PhysRevLett.131.175101 for details on the applied theoretical model, the estimations of other physical processes that affect positron yield and polarization, and the simulation results for other parameters.
[89] A. Alejo, R. Walczak, and G. Sarri, Laser-driven high-quality positron sources as possible injectors for plasma-based accelerators, Sci. Rep. **9** (2019).
[90] Sébastien Corde, E. Adli, J. M. Allen, W. An, C. I. Clarke, C. E. Clayton, J. P. Delahaye, J. Frederico, S. Gessner, S. Z. Green *et al.*, Multi-gigaelectronvolt acceleration of positrons in a self-loaded plasma wakefield, Nature (London) **524**, 442 (2015).
[91] A. J. Gonsalves, K. Nakamura, J. Daniels, C. Benedetti, C. Pieronek, T. C. H. de Raadt, S. Steinke, J. H. Bin, S. S. Bulanov, J. van Tilborg, C. G. R. Geddes, C. B. Schroeder, Cs. Tóth, E. Esarey, K. Swanson, L. Fan-Chiang, G. Bagdasarov, N. Bobrova, V. Gasilov, G. Korn, P. Sasorov, and W. P. Leemans, Petawatt laser guiding and electron beam acceleration to 8 GeV in a laser-heated capillary discharge waveguide, Phys. Rev. Lett. **122** (2019).
[92] Johannes Thomas, Anna Hützen, Andreas Lehrach, Alexander Pukhov, Liangliang Ji, Yitong Wu, Xuesong Geng, and Markus Büscher, Scaling laws for the depolarization time of relativistic particle beams in strong fields, Phys. Rev. Accel. Beams **23**, 064401 (2020).
[93] F. Brunel, Not-so-resonant, resonant absorption, Phys. Rev. Lett. **59**, 52 (1987).
[94] W. L. Kruer and Kent Estabrook, $J \times B$ heating by very intense laser light, Phys. Fluids **28**, 430 (1985).
[95] J. Zhang, Y. T. Li, Z. M. Sheng, Z. Y. Wei, Q. L. Dong, and X. Lu, Fast electrons in high-intensity laser interactions with plasmas, in *Progress in Ultrafast Intense Laser Science II* (Springer, Berlin, Heidelberg, 2007), pp. 319–340.
[96] William H. McMaster, Matrix representation of polarization, Rev. Mod. Phys. **33**, 8 (1961).
[97] Vladimir Borisovich Berestetskii, Evgenii Mikhailovich Lifshitz, and Lev Petrovich Pitaevskii, *Quantum Electrodynamics* (Pergamon, Oxford, 1982).

[98] O. Lundh, F. Lindau, A. Persson, C.-G. Wahlström, P. McKenna, and D. Batani, Influence of shock waves on laser-driven proton acceleration, Phys. Rev. E **76**, 026404 (2007).

[99] G. Doumy, F. Quéré, O. Gobert, M. Perdrix, Ph. Martin, P. Audebert, J. C. Gauthier, J.-P. Geindre, and T. Wittmann, Complete characterization of a plasma mirror for the production of high-contrast ultraintense laser pulses, Phys. Rev. E **69**, 026402 (2004).

[100] Anna Lévy, Tiberio Ceccotti, Pascal D'Oliveira, Fabrice Réau, Michel Perdrix, Fabien Quéré, Pascal Monot, Michel Bougeard, Hervé Lagadec, Philippe Martin, Jean-Paul Geindre, and Patrick Audebert, Double plasma mirror for ultrahigh temporal contrast ultraintense laser pulses, Opt. Lett. **32**, 310 (2007).

[101] Stephen A. Reed, Takeshi Matsuoka, Stepan Bulanov, Motonobu Tampo, Vladimir Chvykov, Galina Kalintchenko, Pascal Rousseau, Victor Yanovsky, Ryousuke Kodama, Dale W. Litzenberg, Karl Krushelnick, and Anatoly Maksimchuk, Relativistic plasma shutter for ultraintense laser pulses, Appl. Phys. Lett. **94**, 201117 (2009).

[102] Sergey Mironov, Vladimir Lozhkarev, Vladislav Ginzburg, and Efim Khazanov, High-efficiency second-harmonic generation of superintense ultrashort laser pulses, Appl. Opt. **48**, 2051 (2009).

[103] Christine A. Aidala, Steven D. Bass, Delia Hasch, and Gerhard K. Mallot, The spin structure of the nucleon, Rev. Mod. Phys. **85**, 655 (2013).

[104] E. G. Gamaly, A. V. Rode, B. Luther-Davies, and V. T. Tikhonchuk, Ablation of solids by femtosecond lasers: Ablation mechanism and ablation thresholds for metals and dielectrics, Phys. Plasmas **9**, 949 (2002).

[105] Y. Y. Ma, Z. M. Sheng, Y. T. Li, J. Zhang, X. H. Yuan, M. H. Xu, Z. Y. Zheng, W. W. Chang, M. Chen, and J. Zheng, Preplasma effects on the emission directions of energetic electrons in relativistic laser–solid interactions, J. Plasma Phys. **72**, 1269 (2006).

[106] A. Pukhov, Z.-M. Sheng, and J. Meyer-ter-Vehn, Particle acceleration in relativistic laser channels, Phys. Plasmas **6**, 2847 (1999).